Advances in Science and Technology Research Journal

Advances in Science and Technology Research Journal, 2026, 20(10), 250–265
https://doi.org/10.12913/22998624/225370
ISSN 2299-8624, License CC-BY 4.0

Received: 2026.05.07
Accepted: 2026.07.10
Published: 2026.09.01

Wireless power transmission integrated into converter for mobile robots

Dao Tuan Anh[1,2], Nguyen The Vinh[1*]

[1] Automation and Robotics Laboratory-ARL Lab, Faculty of Electronic Engineering I, Posts and Telecommunications Institute of Technology Hanoi, Vietnam
[2] College of Agricultural Mechanics, Phu Tho, Vietnam
* Corresponding author's e-mail: vinhnt@ptit.edu.vn

ABSTRACT

This paper investigates a flexible multi-port converter integrated with wireless power transfer (WPT) to provide an efficient power distribution solution for DC microgrids, thereby enhancing operational efficiency in factories employing autonomous mobile robots (AMRs). The proposed converter operates flexibly, supporting both voltage conversion and low-power wireless power transmission. Experimental results demonstrate that the system achieves a conversion efficiency of approximately 94% on the microgrid side and a wireless transmission efficiency of about 73% at 50 kHz, delivering a stable output voltage of 35.3 V and an output power of 25.7 W to the AMR battery. The proposed solution not only reduces downtime caused by battery charging but also improves flexibility and automation in smart factory environments, contributing significantly to the advancement of DC microgrid technologies.

Keywords: DC microgrid, DC/DC converter, WPT, bidirectional converter, hybrid DC/DC.

INTRODUCTION

In recent years, research on DC microgrid (DC MG) structures has developed rapidly to meet the growing demand for efficient power distribution in modern industrial factories [1, 2], particularly in environments employing autonomous mobile robots (AMRs) and mobile robotic systems [3, 4]. Numerous studies conducted have demonstrated that DC microgrids provide significantly higher efficiency than conventional AC grids due to the considerable reduction in AC/DC conversion losses [5-7] and power supply system primarily focused on integrating renewable energy sources, including photovoltaic (PV) systems and wind turbines, into the central DC bus [8, 9]. In industrial factories, DC microgrid architecture enables direct power distribution to wireless charging stations for AMRs. AMRs are used in smart factories and automated warehouses to perform tasks such as material handling, product sorting, and flexible production support. Unlike traditional automated guided vehicles (AGVs), AMRs are capable of self-positioning, path planning, and obstacle avoidance without the need for fixed infrastructure, thereby enhancing flexibility and operational efficiency in modern manufacturing environments. Several studies have deployed DC microgrid systems integrating wireless power transfer (WPT) technology to support the continuous operation of mobile robot fleets [10–12]. However, the continuous operating time of AMRs is still significantly limited by the built-in battery capacity of the robots, reducing productivity and increasing system downtime for charging or battery replacement. This becomes one of the main challenges in deploying large-scale robot fleets in smart factories [13–15].

Currently, most AMR systems use contact charging via mechanical connectors or manual battery replacement. Although this method is highly efficient, mechanical contacts are susceptible to wear, oxidation, and damage in industrial environments with high levels of dust, vibration, and humidity. In addition, physical connections reduce reliability, require periodic maintenance, and cause disruptions to robot operation [16]. To overcome these limitations, wireless power transfer technology, especially Resonant Inductive Power Transfer, has emerged as a promising solution due to its contactless power transfer capability, safety, and complete automation of the charging process [17].

Many recent studies have focused on developing WPT systems for electric vehicles, AGVs, and AMRs. Review works show that WPT technology can achieve transmission efficiency of over 90% under optimal alignment conditions, while completely eliminating mechanical contacts [18]. In addition, studies have proposed various winding structures such as circular, DD, DDQ, and bipolar to improve the anti-displacement capability between the transmitter and receiver [19]. Some other studies focus on optimizing resonance compensation circuits such as SS, SP, PS, and LCC to improve transmission efficiency under varying load conditions [20]. Hassan et al. proposed a resonant transmission system for a medium-sized inspection robot with a power of approximately 100 W; however, the system only considered the independent battery charging process and did not integrate with the multi-port power architecture on the robot [21]. High-power WPT systems for AGVs and AMRs have been developed at kW power levels to meet industrial operating needs, but still mainly use separate converter structures between the wireless charger and the robot's power management unit [22–24]. Subsequent studie in [25, 26] proposed a bidirectional multi-port DC/DC converter architecture for microgrid applications, enabling flexible energy exchange among photovoltaic (PV) sources, battery storage systems, and industrial loads. The research group in [27, 28] developed a multi-port converter incorporating soft-switching technology, achieving efficiencies of up to 96% under highly dynamic load conditions, which are typical in factories utilizing autonomous mobile robots (AMRs). Comprehensive review studies in [29] further emphasized that flexible multi-port converters represent a key solution for energy management in industrial DC microgrids. Reference [30] is among the few studies addressing WPT in mobile microgrids; however, the work was limited to simulation analysis and was not validated in real factory environments.

Despite significant progress, current research still has some considerable gaps: (1) most studies only consider wireless power transmission as a standalone functional block, while AMR power systems in factory environments often require multiple functions simultaneously, such as battery charging, powering drive loads, energy exchange between robots, and connection to micro DC grids. The use of multiple separate power converters increases system size, weight, cost, and losses. (2) very few studies directly integrate WPT functionality into multi-port converter architectures. Existing studies mainly focus on optimizing transmission efficiency without considering the possibility of flexible power sharing between multiple power ports in AMR [16, 17]. (3) in smart factory environments, AMRs often operate continuously in large numbers and require rapid self-recharging capabilities while maintaining high availability. However, current research has not fully addressed the coordination between wireless power transmission, multi-source power management, and fault isolation in the robot's power system. Therefore, it is necessary to study an integrated wireless power transmission converter capable of simultaneously performing multiple power functions on the same hardware structure to reduce the number of power components, increase power density, improve overall efficiency, and enhance the reliability of the AMR system. Stemming from the aforementioned gaps, this study proposes a multi-port converter with integrated wireless power transmission functionality for AMR robots operating in smart factory environments. The converter is designed to simultaneously perform wireless power transmission, multi-source power management, and bidirectional power exchange between power ports on the robot. The main objectives of the research are: (i) to build converter architecture integrated WPT; (ii) to reduce the number of components and power conversion stages; (iii) to improve power transmission efficiency under real-world AMR operating conditions; and (iv) to ensure flexible, continuous, and reliable operation in a smart factory environment.

Figure 1 presents the block diagram of the proposed flexible power converter, which integrates wireless power transfer (WPT) for mobile robots in industrial factories with a DC microgrid system. On the left side of the diagram is the DC microgrid, consisting of multiple input energy sources, including photovoltaic (PV) sources, battery storage systems, and wind energy sources. These sources are connected through DC/DC and AC/DC converters to convert the generated energy into suitable forms before supplying power to the system. The central part of the diagram illustrates the AMR1/AMR2/... WPT three-port converter block, representing a contactless wireless power transfer system that utilizes coupled coils to deliver energy to autonomous mobile robots (AMRs). One port is connected to the AMRs, while another port interfaces with the DC microgrid. Flexible DC/DC converter configurations are employed to regulate voltage and current according to the requirements of both the DC microgrid and the wireless power transmission process. On the right side of the diagram, the AMR1-Bat unit demonstrates the direct battery charging function for the mobile robot. The entire system is designed based on modular architecture, enabling easy integration and scalability for various renewable energy sources. The proposed converter plays a critical role in managing the energy flow from PV, battery (Bat), and wind (Wind) sources to the DC microgrid and AMR1-Bat unit, while simultaneously supporting stable wireless power transfer to actively operating AMRs within the factory environment. With this architecture, mobile robots can receive power continuously without interrupting operation for conventional wired charging.

PROPOSING A SOLUTION FOR THE CONVERTER

The WPT system for AMR1 and AMR2 is based on the principle of high-frequency magnetic resonance combined with direct energy transfer through a DC/DC converter, as illustrated in the power circuit shown in Figure 2. The input DC power is supplied through switches M1 and M2, configured in a bridge converter topology, to the energy storage system of the mobile robot AMR1. Switch M1 operates at the resonant frequency to convert DC power into stable high-frequency AC power. The control circuit of switch S1 employs zero-voltage switching (ZVS) techniques to minimize switching losses. Coil L1 generates a high-frequency magnetic field and stores alternating energy to directly supply power to the AMR1 battery or to transfer energy wirelessly across the air gap to coil L2. Coil L2, mounted on the mobile robot (AMR1/AMR2), receives the magnetic flux and generates an induced electromotive force. The mutual inductance coefficient *M* determines the effectiveness of the wireless coupling and charging performance for AMR1, AMR2, or other AMR systems. The induced energy in L2 is delivered to the compensation network on the receiving side to stabilize the output voltage. The wireless power transfer system utilizes parallel-compensated LC resonant circuits on both the primary and secondary sides. A bridge rectifier consisting of four diodes D1, D2, D3, and D4, together with switch M1, enables bidirectional or unidirectional power transfer depending on the operating mode. Schottky diodes are employed to minimize conduction losses caused by forward voltage drops. The rectified DC power is then processed by a DC/DC converter to regulate the charging current and voltage supplied to the battery. During constant-current charging mode, the charging current is maintained at a fixed value to protect the battery during the initial charging stage. As the battery approaches

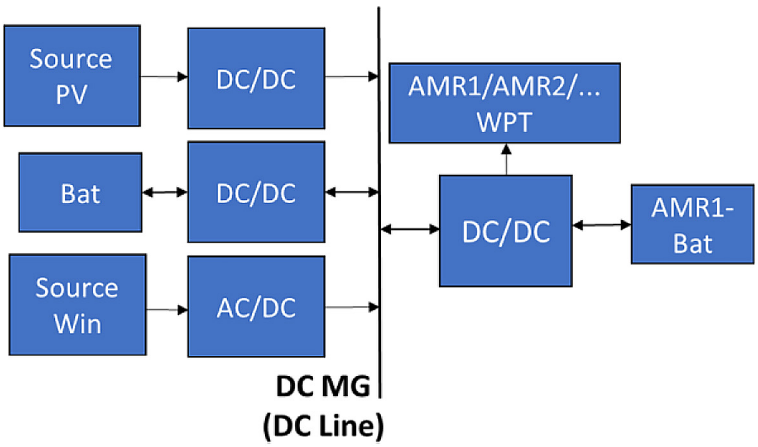

Figure 1. Structural diagram using a flexible converter with a DC microgrid

full charge, the system transitions to constant-voltage charging mode to complete the charging process safely. In addition, the power flow is continuously monitored to detect foreign objects or abnormal conditions between the transmitting and receiving coils.

Misalignment between coils L1 and L2 causes a reduction in the mutual inductance coefficient M [15], which significantly decreases the received power. To compensate for variations in mutual inductance, the robot employs a frequency control algorithm that adjusts the operating frequency dynamically. AMR1 can also potentially operate as a power transfer unit to support the DC microgrid when additional grid power is required. The proposed converter is capable of simultaneously supplying power to multiple AMRs by concentrating magnetic field energy on robots requiring charging. Both coils L1 and L2 are constructed using ferrite materials with circular geometries to reduce electromagnetic interference (EMI) and improve magnetic coupling efficiency. Wireless communication between the charging station and the robots enables coordinated control of the charging start/stop process. The dual-LCC compensation structure allows the system to adapt effectively to impedance variations of the energy storage system installed in the AMRs. Excess switching energy is absorbed by capacitors to protect the power electronic components. Overvoltage and overcurrent protection circuits are integrated immediately after rectifiers D1–D4 for switch M1, and similar protection structures are also implemented for M2. In addition, AMR1 can mechanically adjust the coil position to optimize the coupling coefficient k. The wireless power transfer process between AMR1 and AMR2 can be modeled using a two-port network approach. The reflected impedance from AMR2 to AMR1 is calculated to regulate the output power, as expressed in Equations 1–3. WPT technology enables robots to operate safely in dusty or humid industrial environments. Furthermore, the transmitted power on the primary side is carefully limited to ensure electromagnetic field exposure remains within safety standards for human operators. EMI filter components are installed at the DC input stage to prevent conducted interference from propagating back into the power grid. Wireless charging between AMR1 and AMR2 can also occur while the robots are moving at low speeds. In standby mode, the charging station consumes extremely low power because switch S1 remains completely turned off.

Input impedance of the DC microgrid relative to the AMR1 port.

$$Z_{in,DC\ grid} = sL1 + R_{on(M1)} + \\ + R_{on(M2)} + \left(sCdc2 + \frac{1}{RBat1}\right) \tag{1}$$

The input impedance of AMR1 port is directed towards L2.

$$Z_{in,AMR1} = sL2 + R_{on(M2)} + R_{on(S1)} + \\ + \left(sCdc2 + \frac{1}{RBat1} + \frac{n^2}{sL1 + R_{on(M1)}}\right) \tag{2}$$

The input impedance of AMR2 as seen from the load of AMR2.

$$Z_{in,AMR2} = R_{on(S1)} + \\ + \left(sC + \frac{1}{sL1 + R_{on(M1)}} + \frac{1}{n^2\left(sL2 + R_{on(M2)}\right)}\right) \tag{3}$$

where: s is a variable in the Laplace transform, used to convert the switch from the time domain to the general frequency domain. $s = \sigma + j\omega$; σ – decay portion, $j\omega$ – frequency portion; n – transformer ratio.

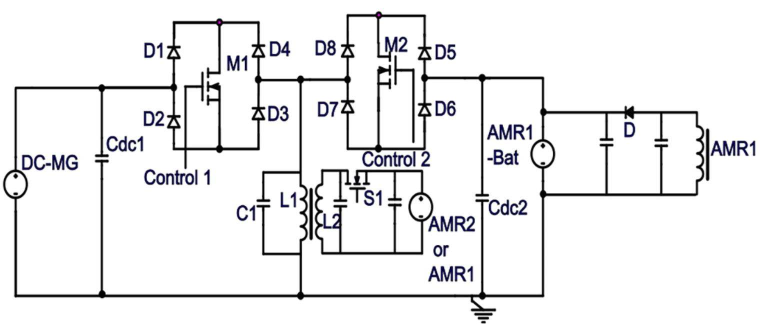

Figure 2. Schematic diagram of the proposed power converter circuit for AMR. Port 1: DC-MG, Port 2: Battery (AMR1-Bat), Port 3: Load (AMR)

Figure 3 illustrates the energy conversion structure used for the AMR1-Bat storage system connected to the DC microgrid charging station, while also managing the battery charging process. The power flow begins from the DC-MG source, which provides a stable input voltage for the charging system. Capacitor Cdc_1 acts as a buffer to suppress high-frequency noise and stabilize the DC bus voltage before the power reaches the semiconductor switching stages. The first main stage consists of switch M1 and diodes D1 and D3, where Control 1 regulates the switching operation of M1 to manage energy transfer through inductor L_1. Inductor L_1 and capacitor C_1 form a resonant or filtering network depending on the operating mode, enabling continuous energy storage and release to maintain a stable charging current. A notable feature of the proposed structure is that L_1 functions both as a wireless power transfer coil and as a current-filtering inductor during direct charging operation, thereby reducing system size and weight.

When M1 is turned on, energy from the DC-MG is stored in L_1. When M1 is turned off, current continues flowing through freewheeling diodes D1 and D3, ensuring continuous power delivery and protecting the semiconductor devices from voltage spikes. The second switching stage, including M2 and diodes D6 and D8, regulates the charging voltage and current according to the AMR1-Bat requirements. Control 2 adjusts the switching duty cycle of M2 to implement constant-current charging during the initial stage and constant-voltage charging when the battery approaches full capacity. Diodes D6 and D8 prevent reverse current flow from the battery to the converter, ensuring safe operation during power interruptions. The output capacitor Cdc_2 smooths the regulated energy and provides stable DC power to the battery, reducing voltage ripple and improving charging efficiency. In addition, the coordinated operation of L_1, C_1, and the MOSFET parasitic capacitors enables zero-voltage switching (ZVS), reducing switching losses and electromagnetic interference (EMI). The proposed topology also supports flexible impedance adaptation and maximum power point tracking, allowing the AMR1 system to optimize charging conditions based on the battery state of charge (SoC). Overall, the proposed circuit functions as an intelligent energy management system that enables efficient and autonomous operation of AMR-based robotic systems in smart factory environments.

The schematic diagram of the wireless power converter and transmission system, illustrated in the operating case shown in Figure 4, is specifically designed for AMR1 and AMR2 mobile robots with flexible power transfer capability. The power supply originates from the DC microgrid, which acts as the main energy source providing stable power for the entire charging process. Capacitor Cdc_1 is connected in parallel with the input source to suppress AC ripple and stabilize the DC bus voltage before the inverter stage. The high-frequency inverter stage consists of the resonant circuit formed by L_1 and C_1, together with power switch M1, which is optimized according to the charging power requirements of the AMRs. Switch M1 is controlled by "Control 1" and operates at high switching frequency to convert DC power into high-frequency AC power. The operating frequency of M1 is designed to match the resonant frequency of the system in order to maximize wireless power transfer efficiency. Coil L_1, combined with capacitor C_1, forms the primary resonant network responsible for generating a strong alternating magnetic field. This magnetic field propagates through the air gap and creates mutual induction with the secondary coil

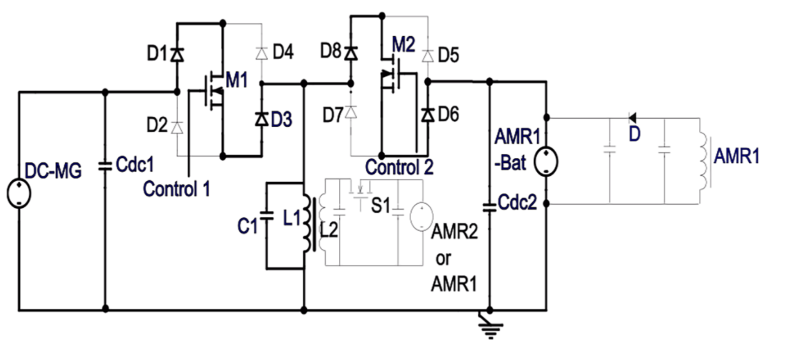

Figure 3. Schematic diagram of AMR1 power mode being charged directly from the DC microgrid

L_2 mounted on the mobile robot, enabling contactless energy transfer. On the receiving side, highlighted in bold in the diagram, coil L_2 and its corresponding resonant circuit efficiently capture the transmitted magnetic flux. Switch S1 plays an important role on the receiving side and is commonly used as a charging control switch or for resonance compensation purposes. The received energy is filtered by capacitor C at the AMR2 load side to smooth the voltage and convert it into stable DC power for supplying the AMR2 battery, AMR1 battery, or other AMR systems. A unique feature of the proposed structure is its capability to transfer transient energy through switch S1 and the final output coil located on the right side of the diagram. Diode D prevents reverse current flow from auxiliary loads, ensuring unidirectional energy transfer to the subsequent robot or AMR2 load system. In addition, zero-voltage switching (ZVS) is achieved through precise coordination between the inductive and capacitive components and the switching timing of M1. The implementation of ZVS significantly reduces switching losses and thermal stress on M1, thereby enhancing both converter efficiency and component reliability.

The total impedance AMR2, viewed from the end of L1, transmits wireless energy when the load is storage.

$$Z_{in,AMR2} = R_{on(S1)} + \\ + \left(sC + \frac{1}{sL1 + R_{on(M1)}} + \frac{1}{n^2\left(sL2 + R_{on(M2)}\right)} + \frac{1}{RBat2} \right) \quad (4)$$

Figure 5 presents a WPT system combined with direct power transfer for alternating charging of AMR1 and AMR2 mobile robots. The system is powered by a DC microgrid source providing a stable DC voltage of 100–200 V. The transmitter consists of a single-switch resonant inverter using M1, D1, D3, and the resonant network L_1-C_1. The switching of M1 is controlled to achieve soft switching, while the resonance of L_1-C_1 transfers energy inductively to the secondary circuit L_2-C_2.

When M1 conducts, energy from the DC source charges the primary inductor L1. When M1 is switched off, the current in L1 cannot change abruptly; it begins to resonate with capacitor C1, forming a harmonic oscillation network.

The equation characterizing the resonant frequency of the generator circuit is

$$f = \frac{1}{2\pi\sqrt{L1C1}} \quad (5)$$

The coil L1 then generates a strong varying magnetic field, propagating through the air gap. This magnetic field energy is absorbed by the secondary coil L2 located on the robot AMR2 through the mutual inductance coefficient M. At the receiving end, AMR1-Bat, it is converted through M2 and diodes D6 and D8 during the conduction time of M2. When Control 2 detects that the AMR1-Bat battery is full or needs power flow regulation, it activates S1 to change the control of Control 2 accordingly. However, the most unique aspect of this bolded diagram is its ability to transmit relay energy. Diode D acts as a barrier to prevent reverse current flow from the subsequent stages back to the battery of AMR1, ensuring consistency and safety for the DC power flow. Mathematically, the transmitted power P depends closely on the coefficient k and the quality factor Q of the windings, expressed by the formula $P \in \omega MI1I2$ is the angular frequency of oscillation. The conditional coordination (9–10) between semiconductor components such as M1, M2, and S1 and diodes D1–D8 along with passive components L and C has created a self-sustaining energy ecosystem.

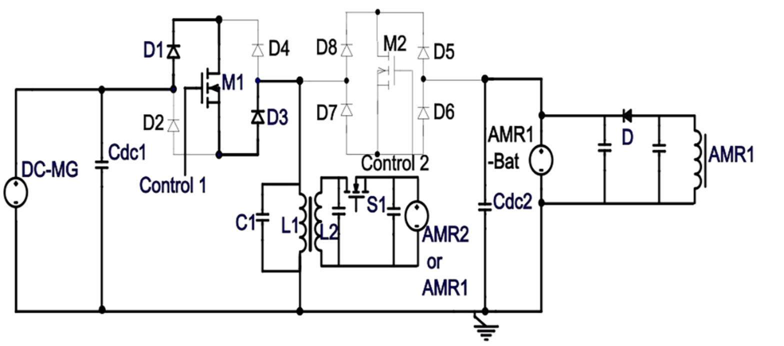

Figure 4. Schematic diagram of AMR1 or AMR2 power mode being wirelessly charged from a DC microgrid

The transformer coupling coefficient characterizes the magnetic connection between two windings L1 and L2, related to mutual inductance M according to the formula.

$$k = M\sqrt{L1L2} \tag{6}$$

The quality factor at coil ports L1 and L2 is determined.

$$Q1=\frac{\omega_0 L1}{R1} \tag{7}$$

where: ω_0 is the resonant angular frequency L1; R1 coil resistance L1.

The efficiency of energy transfer from coil L1 to L2 is established as an efficiency ratio.

$$\eta = \frac{P_{ARM2-Bat}}{P_{DC\ grid}} \approx \frac{k^2Q1Q2}{1+k^2Q1Q2} \tag{8}$$

where: $Q2$ is the quality coefficient of the $L2$ gate determined similarly to expression (7).

The conditional expressions controlling switches S1, M1, and M2 are:

- In the case where only switches M1 and M2 (energy converted from two DC microgrid ports with AMR1) are working, the same duty cycle is used in Control 1 and 2, and the same duty cycle D1 is adjusted accordingly so that the voltage and power current are suitable for the two ports with different voltage values and have a relationship as shown in expression (9).

$$VBat1 = \frac{D1}{1-D1}V_{DC\ grid} \tag{9}$$

- In the case where M1 or M2 and S1 (operating in relation to two DC microgrid ports and AMR2, AMR1) are working together, the duty cycle of M1 and S2 is D2 because the power current in this case is smaller due to wireless energy transmission according to the expression (10).

$$VBat2 = \frac{D1}{1-D1}nV_{DC\ grid} \tag{10}$$

- In the case where M1, M2, and S1 (operating in relation to the two DC microgrid ports AMR1 and AMR2) are working together, the duty cycle of M1 and M2 is D1, and that of S1 is D2. Because the output is two and the input is one, the duty cycle will be longer when the required output energy is greater, and vice versa.

Figure 6 illustrates the operating modes when AMR1 receives power from the DC microgrid. In Mode 1, the wireless power transfer system is inactive, and the converter operates through direct power transmission from AMR1. The received AC power is converted to DC through diodes D5–D8 and switches M1 and M2, which operate as a synchronous rectifier to reduce voltage loss and improve efficiency at low power levels. Control 1 and Control 2 generate precise gate signals with dead-time protection to prevent shoot-through. In Mode 2, AMR1 wirelessly transfers power to AMR2 while switch M1 remains inactive. In Mode 3, AMR1 simultaneously supplies power to both the DC microgrid and AMR2. The operating principle is similar to the previous converter mode, but with a higher output voltage. The proposed design ensures stable operation even at low power levels of only a few tens of watts. In addition, feedback from the DC microgrid allows the control loop to quickly regulate the output voltage, ensuring a continuous and reliable power supply for mobile robots.

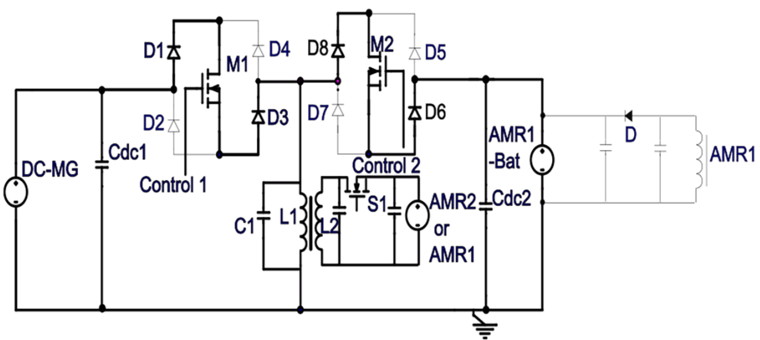

Figure 5. Schematic diagram of the case where AMR1 is charged directly from the DC microgrid and AMR2 is charged wirelessly

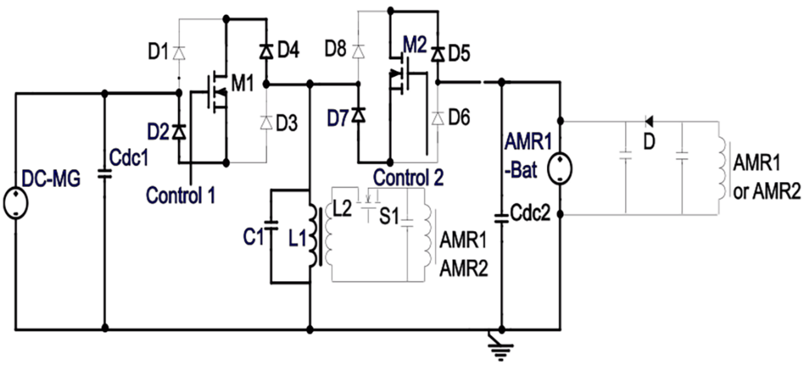

Figure 6. DC microgrid or AMR2 energy received from AMR1 storage

The mathematical model for frequency modulation-based control of the converter has three specific cases as follows:

- This case involves direct power transfer using two DC microgrid ports and AMR1.

$$P_{SW} = \frac{1}{2} V_{DC\ grid} . I_{AMR1-Bat} [t_{off} + t_{on}] f_{sw} \tag{11}$$

$$f_{PFM} = \frac{2 I_{AMR1-Bat} L1}{t_{on} V_{DC\ grid} \left(1 - \frac{V_{AMR1-Bat}}{V_{DC\ grid}}\right)} \tag{12}$$

- Case of wireless power transmission with DC grid voltage control and transfer function.

$$G(s) = \frac{v_x(s)}{f(s)} \tag{13}$$

where: $v_x(s)$ is the voltage at the three-branch connection L1, M1, and M2 in the proposed converter. The general control model controls the frequency for the ports considered as outputs or loads.

$$C \frac{dv_x}{dt} = P(f) - P_{Bat} \tag{14}$$

Power is related to frequency.

$$\frac{\partial P}{\partial f} = 2\pi M I1 I2 sin\alpha \tag{15}$$

where: α is the angle between the two currents I1 and I2 flowing through coils L1 and L2.

Control to maintain stability v_x

$$f = f_0 + K_p(V_{ref} - v_x) \tag{16}$$

where: f_0 is the initial frequency when performing frequency modulation; *Kp* is the proportionality constant in the control model.

SIMULATION ANALYSIS

Figure 7 presents the simulated relationship between the switching frequency of M1 and M2 and the charging voltage of the AMR robots. The switching frequency ranges from 20 kHz to 80 kHz, which is suitable for optimizing the size of magnetic and power electronic components. In the proposed converter, the wireless power transmission circuit uses a parallel LC resonant circuit, often preferred on the power generation side of the robot's storage load to generate a large current flowing through the coil. The analysis and selection of the resonant frequency is based on factors affecting power reception and transmission efficiency, specifically the LC resonant circuit quality factor as expression (7). A quality factor value of Q = 5–10 allows for easy adaptation of the system without the need for overly complex or expensive frequency-track controllers. Performance remains stable even when the robot is parked off-center, resulting in a higher total daily energy charge. The charging voltage of AMR1 and AMR2 varies from 20–100 VDC for DC microgrid input voltages of 100 VDC and 200 VDC. The results show that the charging voltage increases nonlinearly with switching frequency. At a 100 VDC input, the charging voltage rises from approximately 20 V at 20 kHz to about 52 V at 80 kHz. For a 200 VDC input, the charging voltage increases from around 42 V to approximately 102 V over the same frequency range. The steeper slope at 200 VDC indicates greater sensitivity of the output voltage to frequency variation at higher input voltages. In general, doubling the DC-MG input voltage nearly doubles the AMR charging voltage, confirming the proportional relationship between the input and output voltages. The nonlinear characteristics are caused by the

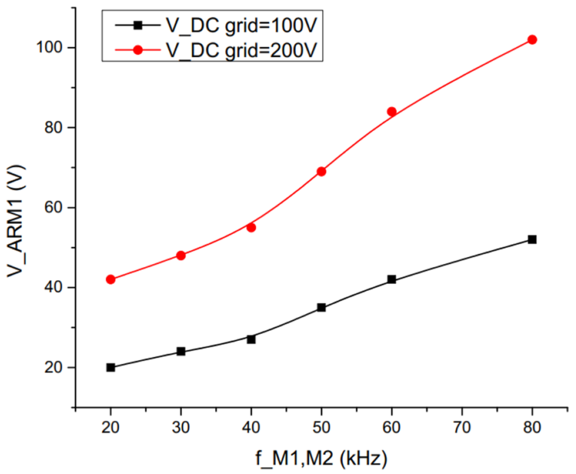

Figure 7. Effect of frequency on the charging voltage for AMR1 from the DC-MG grid

resonant compensation network, whose voltage gain depends on the operating frequency. Therefore, frequency modulation of M1 and M2 is used to regulate the charging voltage and maintain constant-current and constant-voltage charging modes for lithium batteries. The results also demonstrate that increasing the switching frequency is an effective method for fast charging. The close agreement between the simulation points and the fitted curves confirms the accuracy of the mathematical model and converter design. In addition, high-frequency operation allows smaller coils and capacitors while maintaining ZVS soft-switching conditions for M1 and M2. The wide voltage regulation range enables compatibility with various AMR battery voltage levels without requiring hardware modifications, making the system suitable for continuous operation in smart factory and warehouse environments.

Based on the graph in Figure 8 and the analyzed circuit diagrams, the switching frequencies of M2 and S1 significantly affect the charging voltage of AMR2 when power is wirelessly transferred from AMR1. The graph shows a positive nonlinear relationship between the switching frequency range of 20–80 kHz and the AMR2 charging voltage for AMR1 battery voltages of 36 VDC and 48 VDC. For the 36 V configuration, the charging voltage increases from approximately 16 V at 20 kHz to about 22 V at 80 kHz. In the 48 V configuration, the charging voltage rises from around 25.5 V at 20 kHz to approximately 32.5 V at 80 kHz, maintaining a voltage difference of about 10–12 V across the entire frequency range. The nonlinear characteristics of the curves reflect the gain behavior of the resonant compensation network, which depends on the operating frequency. Therefore, frequency modulation of M2 and S1 is used to regulate the output voltage and adapt the system impedance according to the battery charging state. In addition, coordinated switching between M2 on the transmitter side and S1 on the receiver side improves magnetic flux transfer efficiency from AMR1 to AMR2. The simulation results confirm that the proposed WPT system can flexibly support different AMR battery voltage levels while maintaining stable charging performance.

Observing Figure 9, it is clear that frequency has a significant influence on the wireless charging voltage at AMR1 and AMR2. In the case of $V_{DC-grid}$ = 200, the charging voltage increases noticeably as the switching frequency rises. At low frequencies, the charging voltage starts at a relatively low level and gradually increases along a nonlinear curve. As the frequency continues to increase, the charging voltage rises more rapidly, approaching a nearly linear trend at higher frequencies. This behavior indicates that the magnetic coupling efficiency between coils L_1 and L_2 improves with increasing frequency. As a result, both the AMR1 output voltage and the AMR2 charging voltage are significantly enhanced.

Compared with previous measurements at 50 kHz, increasing the switching frequency directly improves the battery charging voltage. Therefore, Control Units 1 and 2 must dynamically regulate the operating frequency to maximize the voltage gain while ensuring that M1 and M2 maintain soft-switching operation. The graph also

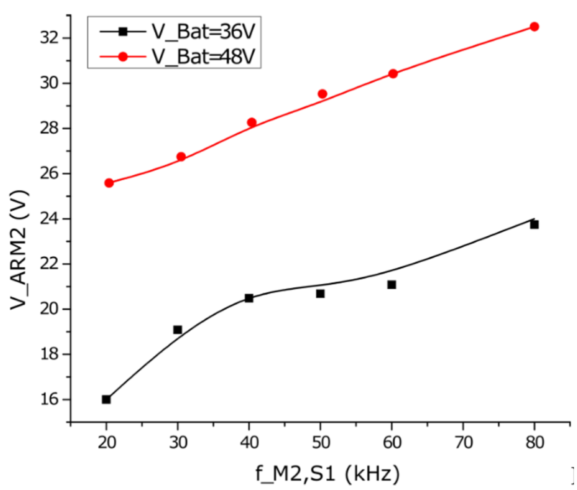

Figure 8. Effect of frequency on wireless voltage at AMR2 charging head

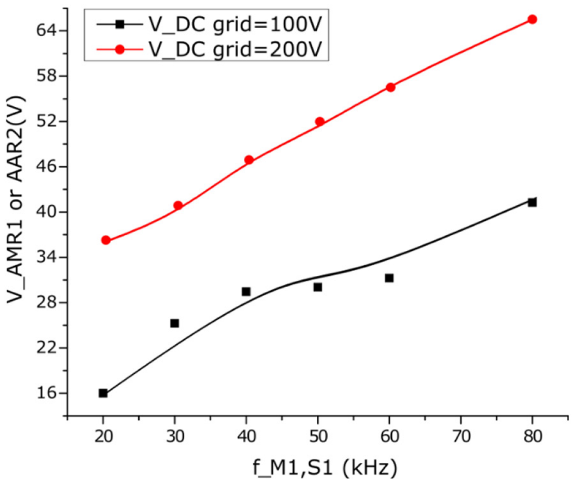

Figure 9. Effect of frequency on wireless voltage at AMR1 or AMR1 charging hea

indicates that energy transfer efficiency decreases at low frequencies because the coil impedance has not reached its optimal resonant condition. In IoT-based DC microgrid applications, proper frequency selection is essential for maintaining stable wireless charging voltage for mobile robots. Figure 10 further confirms that frequency is a key parameter directly affecting the wireless charging performance of AMR1 and AMR2.

Figure 10 (a) presents the simulated influence of the switching frequencies of M1, M2, and S1 on the power transmission efficiency of the AMR1 and AMR2 systems. The graph evaluates four operating modes: DC grid-to-AMR1 charging, reverse power transfer from AMR1 to the DC grid, simultaneous charging of AMR1 and AMR2, and AMR1-to-AMR2 relay charging. Overall, the efficiency of all modes decreases as the switching frequency increases from 20 kHz to 80 kHz. This reduction is mainly caused by switching losses in M1, M2, and S1, reverse recovery losses of diodes D1–D4, and increased parasitic and ferrite core losses in coils L_1 and L_2. The DC grid-to-AMR1 mode achieves the highest efficiency, decreasing from approximately 98% at 20 kHz to 94.5% at 80 kHz due to the optimized direct charging structure. The reverse AMR1-to-DC grid mode maintains efficiencies between 95.5% and 93.5%, demonstrating stable bidirectional power transfer capability. The simultaneous charging mode for AMR1 and AMR2 shows lower efficiency, dropping from 91% to about 84% as the frequency increases because of higher current stress and additional magnetic coupling losses.

The AMR1-to-AMR2 relay charging mode exhibits the lowest efficiency, ranging from 75.5% to 72.5%, since the energy passes through two wireless transfer stages. Although this relay mode has lower efficiency, it remains important for supporting robots operating outside the fixed charging station coverage area. At the standard operating frequency of 50 kHz, the efficiencies of the four modes are approximately 96%, 94.5%, 84.5%, and 74%, respectively. The results confirm that increasing frequency helps reduce component size but also increases switching losses and thermal stress on the power devices. The close agreement between the simulated points and trend lines validates the accuracy of the mutual inductance model and coupling coefficient design. Overall, the proposed WPT relay system demonstrates the potential for energy-sharing robot swarms capable of long-term autonomous operation in smart factory environments.

Figure 10(b) presents the simulated effects of the duty cycle D of switches M1, M2, and S1 on the power transmission efficiency of the AMR1 and AMR2 systems. All operating modes show a similar trend in which efficiency is highest at low duty cycles and gradually decreases as D increases. In the region of $D < 0.5$, single-stage transmission modes such as DC grid-AMR1 and AMR1-DC grid maintain efficiencies above 95%, indicating that soft-switching conditions are effectively achieved and conduction losses remain low. However, when $D < 0.5$, the efficiencies of these modes decrease rapidly to approximately 72–73% at $D = 0.9$ due to increased conduction time and higher current stress on switches M1 and M2, leading to greater thermal losses in coils L_1, L_2, and the semiconductor devices. The simultaneous charging mode for AMR1 and AMR2 starts at about 91% efficiency but decreases more rapidly because the shared magnetic flux changes the equivalent impedance seen by the inverter stage. At $D = 0.4$, the efficiency drops to around 80%, showing the sensitivity of multi-load operation to duty cycle variations. The AMR1-AMR2 relay charging mode exhibits the lowest efficiency, decreasing from approximately 73% to 54% at $D = 0.9$, since the energy passes through two wireless transmission stages and two resonant networks. Despite its lower efficiency, this Robot-to-Robot (R2R) mode remains important for supporting robots operating outside the charging station coverage area. The simulation results closely

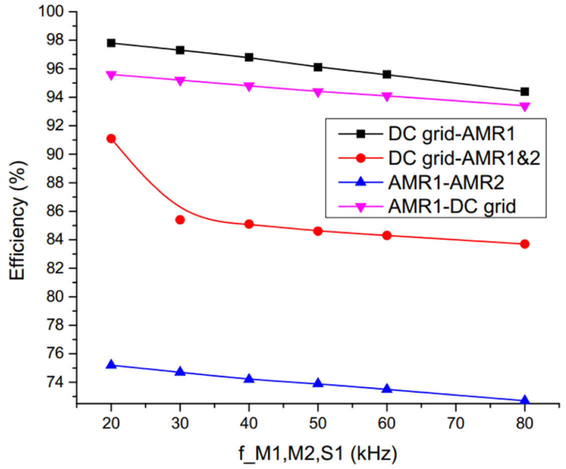

(a)

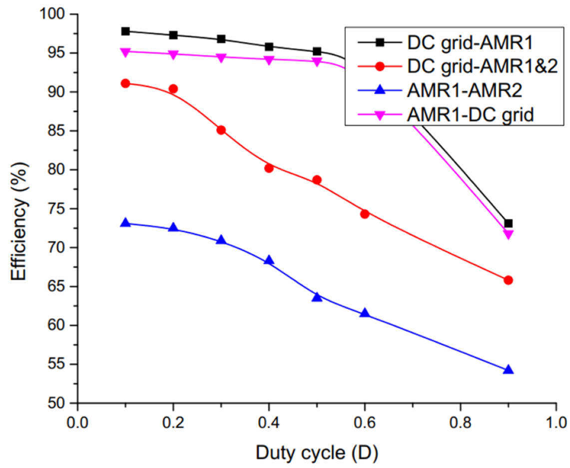

(b)

Figure 10. Parameter effects on converter performance: (a) switching frequency, (b) proposed converter switchs duty cycle

follow the trend curves, confirming the stability of the single-switch resonant inverter design. The analysis indicates that the optimal operating range for the AMR swarm is within $D = 0.1$ to 0.3, where the balance between power transfer capability and energy efficiency is most suitable for autonomous operation. In addition, combining duty cycle control with frequency modulation provides a flexible dual-parameter control strategy for Control Units 1 and 2. Proper duty cycle management is therefore essential for preventing overheating, maintaining high efficiency, and supporting intelligent Robot-to-Grid (R2G) and Robot-to-Robot (R2R) energy-sharing operations in smart factory environments.

Figure 11 illustrates the effect of the distance between coils L_1 and L_2 on the power transmission efficiency of the AMR1 and AMR2 systems. The graph shows an inverse relationship between transmission distance and efficiency for two operating cases: DC grid-to-AMR2 charging and AMR1-to-AMR2 relay charging. In both cases, efficiency decreases as the distance between the coils increases due to the reduction in the mutual inductance coefficient M and coupling coefficient k, which increases magnetic flux leakage. At a short distance of approximately 2 cm, the AMR1-AMR2 relay mode achieves the highest efficiency of about 87.5%, slightly higher than the 85% efficiency of direct grid charging. This indicates that the proposed resonant converter structure using switches M1, M2, and S1 is highly effective for robot-to-robot energy transfer. However, as the distance increases to 5 cm, the efficiencies of both modes converge to around 80%. Beyond 6 cm, the relay charging efficiency decreases more rapidly because of accumulated losses through multiple wireless transmission stages. At 8 cm, the DC grid-AMR2 efficiency remains near 68%, while the AMR1-AMR2 mode decreases to approximately 66%. At the maximum tested distance of 10 cm, the grid charging efficiency is about 65%, whereas the relay mode drops significantly to around 60%. Misalignment between the mobile robots further increases transmission losses at larger distances. The analysis confirms that the optimal operating range for maintaining efficiencies above 80% is when the distance between L_1 and L_2 is below 5 cm. Control Units 1 and 2 regulate the switching frequency and duty cycle D to compensate for impedance variations caused by distance changes. The results also demonstrate the feasibility of relay wireless charging for robot swarms in smart warehouse environments while highlighting the importance of accurate robot positioning and short charging distances to maintain high efficiency and reduce charging time.

EXPERIMENT AND DISCUSSION

Figure 12 presents an experimental prototype of the proposed converter system integrating wireless power transfer for an AMR in a laboratory environment. The input parameter settings are shown in table 1. The system is powered by a 36.1 V DC microgrid source connected to a central DC/DC converter board. Two flat copper coils are arranged to demonstrate wireless power transmission from the transmitter coil

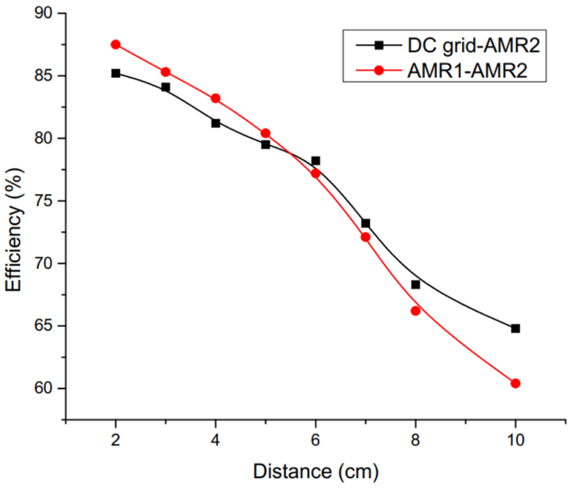

Figure 11. Effect of distance on performance of each mode and average of the proposed converter

on the floor to the receiver coil mounted underneath the AMR. A 16×2 LCD module displays real-time operating parameters. The converter, equipped with a large heat sink, performs synchronous conversion and rectification to ensure high efficiency under DC microgrid operation. The AMR is positioned on the right side of the setup, receiving power wirelessly without physical connections. The entire experimental model clearly demonstrates the processes of DC power supply, wireless transmission, rectification, and energy delivery to the robot in conditions such as workshops and warehouses in the documents [13]. Measurements from the LCD and oscilloscope confirm stable system operation. The prototype validates the integration of WPT technology into a flexible converter system for efficient energy management of AMRs in DC microgrid environments while enabling accurate real-time monitoring during experiments.

In the practical experiment, the flexible converter was tested under two operating scenarios, as shown in Figure 13(a), corresponding to direct charging of AMR1 from the DC microgrid. In the first case, the LCD displays the DC microgrid parameters: V_{DC} = 110.1 V, I = 0.32 A, and P = 35.2 W, confirming stable power delivery from the DC grid. In the second case, the LCD shows the charging parameters of the AMR1 battery: 35.9 V, 0.93 A, and 33.3 W, indicating successful energy conversion to a suitable charging level. The difference between the input power of 35.2 W and the output power of 33.3 W corresponds to a converter efficiency of approximately 94.6%, demonstrating low losses due to synchronous rectification and ZVS operation. The results confirm stable converter performance for both the high-voltage DC microgrid side and the low-voltage battery charging side.

Figure 13(b) presents the wireless charging experiment from the DC microgrid to AMR2. Under the same DC microgrid conditions of 110.1 V, 0.32 A, and 35.2 W, the wireless power transfer system delivered 35.3 V, 0.73 A, and 25.7 W to the AMR2 battery after transmission through the wireless coils and converter stages. The decrease from 35.2 W to 25.7 W indicates a wireless transmission efficiency of approximately 73%, which is acceptable considering the coil distance and copper losses. The results verify the converter's capability to wirelessly transfer and regulate power from the DC microgrid to AMR2 with stable operation over a transmission distance of approximately 6 cm (Table 1).

Based on Figure 14(a), a comparative analysis between simulation and experimental results was conducted for the DC microgrid power conversion system supplying AMR1 and AMR2 robots.

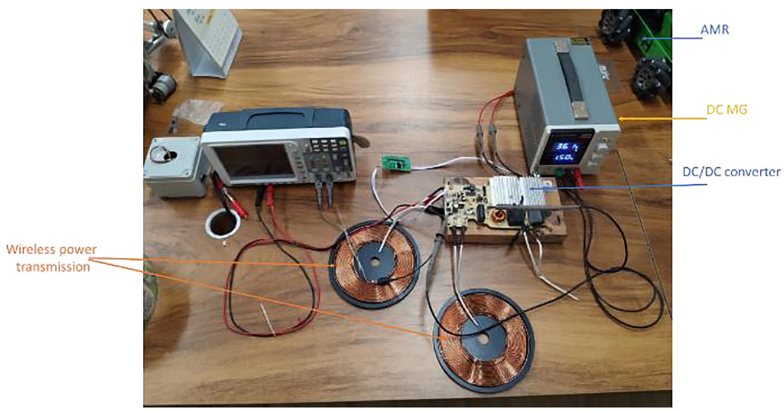

Figure 12. Experimental images in the laboratory

Table 1. Input parameters for experimental modeling of the proposed converter.

Components in the converter	Parameter
Inductor L1, L2	35.5 nH, 28.5 uH, copper wire electrical section Φ=1.5 mm, number of turns L1: 12 turns, number of turns L2 11 turns
Capacitor C1	135 uF
Capacitor Cdc	10 uF
Capacitor C	146 uF
Frequency switch	50–70 kHz
Switch M1, M2	IRF154
Switch S1	IRF110
AMR1-Bat	36 V, 48 V, 2 Ah
AMR transport load	10 kg
AMR movement speed	2.5 m/s
Robot size	39 × 30 × 20 cm
DC-grid	100 V, 200 V

The graph illustrates the relationship between transmission power and efficiency for four operating modes. In all cases, efficiency reaches its highest value at low power levels and gradually decreases as the output power increases due to higher conduction and switching losses in the coils and semiconductor devices. Experimental efficiencies are consistently 1–2.5% lower than simulation results because of practical parasitic losses and non-ideal connections.

For the single charging mode (DC grid-AMR1), the simulated efficiency starts at approximately 98% and remains around 94% at 2000 W, while the experimental results closely follow the simulation with efficiencies decreasing from 97% to 93.5%. This confirms that the resonant compensation network and converter design successfully maintain ZVS operation for M1. In contrast, the simultaneous charging mode for AMR1 and AMR2 exhibits a more significant nonlinear efficiency reduction. At 300 W, the experimental efficiency remains around 90.5%, but a sharp drop occurs in the 500–600 W range, where efficiency decreases from 88.5% to 83.5%. This reduction is caused by increased load demand, impedance variation, leakage inductance, and additional reactive power generated between the receiving coils of AMR1 and AMR2. At the maximum power level of 2000 W, the simultaneous charging efficiency decreases to approximately 74% in both simulation and experiment, indicating that switching losses dominate at high power conditions. The close agreement between simulation and experimental curves confirms the accuracy of the mutual inductance M and coupling coefficient k models. The results also demonstrate that flexible adjustment of switching frequency f and duty cycle D helps maintain optimal efficiency in the 300–500 W operating range. Although relay wireless charging introduces additional losses, the proposed WPT system still achieves experimental efficiencies above 92% in single charging mode, demonstrating high performance and practical feasibility for mobile robot applications in smart factory environments.

Figure 14(b) compares simulation and experimental results for wireless power transfer between AMR1 and AMR2. Two operating cases are analyzed: DC grid-to-AMR2 charging and AMR1-to-AMR2 relay charging. In all cases, the transmission efficiency decreases as the output power increases from 50 W to 200 W due to higher copper and switching losses in M1 and S1. Simulation results remain slightly higher than experimental results because practical effects such as parasitic resistance and electromagnetic interference are not fully considered. For the AMR1-AMR2 relay charging mode, the simulated efficiency decreases

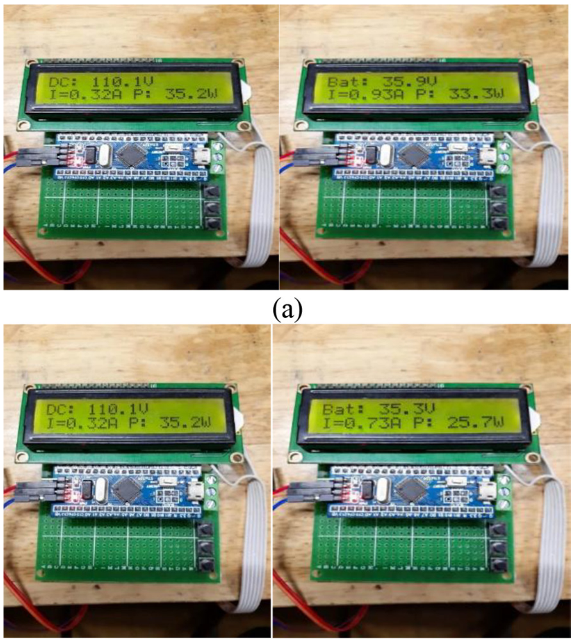

(b)

Figure 13. Measurement and testing model images: (a) DC grid power supply to AMR1-Bat via direct connection, (b) DC grid power supply to AMR1-Bat via wireless connection at a distance of 6 cm

from 86.1% to 81.2%, while the experimental efficiency drops from 85.2% to 75.1%. In the DC grid-AMR2 charging case, the simulated efficiency decreases from 84.5% to 78.6%, whereas the experimental efficiency decreases from 82.6% to 74.3%. The higher relay efficiency in the 50–150 W range demonstrates effective coupling between the two robots. In addition, switch S1 helps maintain ZVS operation and stable efficiency under high-load conditions.

Figure 14(c) compares simulation and experimental results for the wireless power transfer converter with transmission distance as the main parameter affecting performance. All curves show a similar trend in which efficiency decreases as the distance between coils increases due to the reduction of the coupling coefficient *k* and increased magnetic flux leakage. At the shortest distance of 2 cm, the system achieves peak efficiencies between 84.5% and 87.5%, with the simulated AMR1-AMR2 relay mode showing the best performance. The experimental relay results closely match the simulations at distances from 2–6 cm but decrease more rapidly at larger distances because of thermal losses and coil misalignment. Around 5 cm, all operating modes converge near the 80% efficiency level, representing the most stable operating region for the robot system. Beyond 6 cm, the efficiency decreases nonlinearly due to resonant magnetic field characteristics. The simulated DC grid-AMR2 mode maintains the best long-distance performance, reaching approximately 65% efficiency at 10 cm, while the experimental results for both direct and relay charging decrease to around 60%. In the proposed converter, experimental values consistently decreased compared to simulations. This is due to the influence of parasitic elements in the switching mechanism, the resonant frequency deviation from the switching frequency, and the distance and eccentricity of the transceiver coils caused by robot oscillation. In the experiment, the robot was considered stationary, so the eccentricity was considered negligible. Therefore, the optimal distance between the two coils for efficient power transmission was less than 5cm, corresponding to precise position control with an error of a few millimeters for the robots. To compensate for the reduced coupling, switches M2 and S1 regulate frequency and resonance conditions to maintain ZVS operation and stable power transfer. The results confirm that the proposed WPT system can maintain acceptable efficiency even at larger

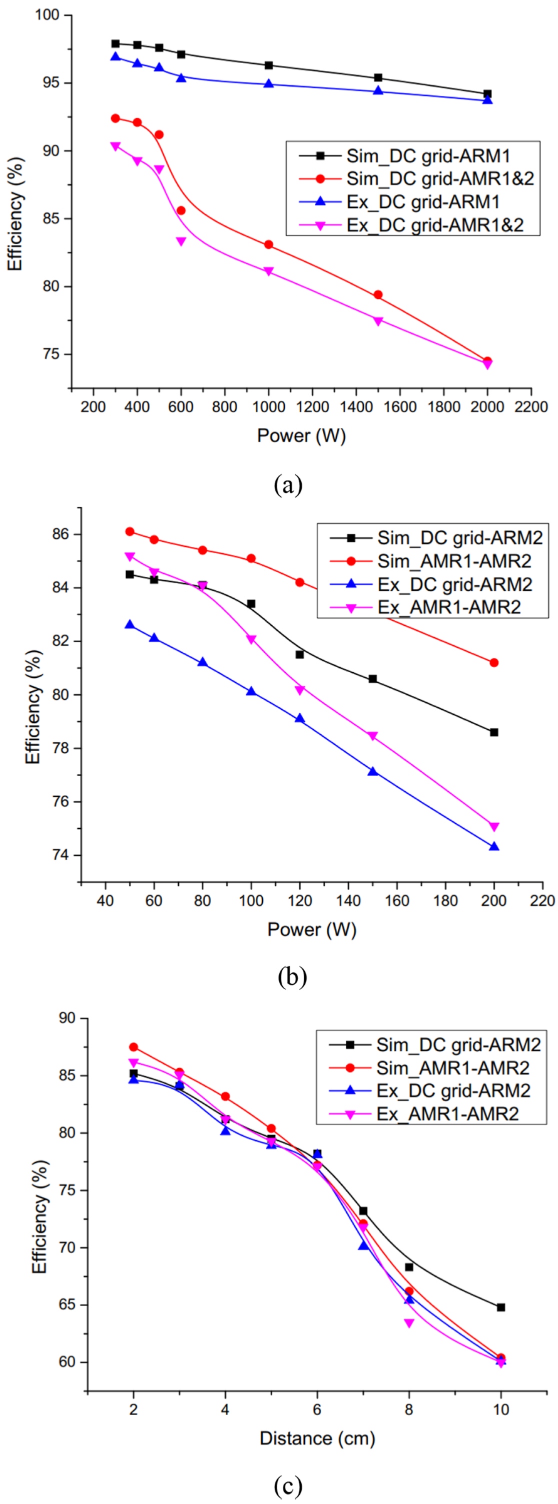

Figure 14. Experimental-simulated comparison of the proposed converter in a DC microgrid for a factory using AMR: (a) direct and wireless power transmission cases, (b) wireless power transmission cases, (c) distance affecting performance

coil distances, supporting flexible wireless charging and energy-sharing operation for AMR systems in smart factory environments.

CONCLUSIONS

The proposed wireless power transfer converter for AMR1 and AMR2 demonstrates high performance, flexibility, and strong practical applicability in modern industrial environments. By employing a single-switch resonant inverter structure, the converter reduces system size and weight while achieving soft-switching operation, thereby minimizing switching losses and electromagnetic interference (EMI). Experimental results confirm direct transmission efficiency above 94.5%, combined transmission efficiency above 82.5%, and wireless transmission efficiency exceeding 79%, demonstrating stable and energy-efficient operation over extended periods. The converter also supports flexible voltage regulation and multiple charging modes, ensuring safe operation for Lithium-ion battery systems. In addition, the relay transmission mechanism enables AMR1 to share energy with AMR2, extending the operating range of the robot swarm beyond the direct coverage area of the DC microgrid. The detuning control technique using switch S1 effectively regulates power flow, prevents overcharging, and optimizes magnetic field utilization for robots requiring higher power. Furthermore, frequency modulation and duty cycle control allow the system to maintain stable performance under coil misalignment and air-gap variations. The integration of wireless charging significantly reduces charging downtime and enhances the autonomy of AMR systems, making the proposed converter a promising energy solution for smart factories and autonomous logistics centers.

Acknowledgment

The research team would like to thank the Automation and Robotics Laboratory-ARL, Posts and Telecommunications Institute of Technology Hanoi, Vietnam for creating favorable conditions during the implementation of the research content of this article.

REFERENCES

1. Al-Ismail FS. DC Microgrid Planning, Operation, and Control: A Comprehensive Review. in IEEE Access 2021; 9(7): 36154–36172. https://doi.org/10.1109/ACCESS.2021.30628408
2. Ashok Kumar A and Amutha Prabha N. A comprehensive review of DC microgrid in market segments and control technique. Heliyon 2022; 8: e11694. https://doi.org/10.1016/j.heliyon.2022.e1169410
3. Shili M, Hammedi S, Chaoui H and Nouri K. Energy-aware swarm robotics in smart microgrids using Quantum-11 inspired reinforcement learning. Electronics 2025; 14(21): 4210. https://doi.org/10.3390/electronics14214210
4. Shili M, Chaoui H and Nouri K. Energy-aware sensor fusion architecture for autonomous channel robot navigation in constrained environments. Sensors 2025; 25: 6524. https://doi.org/10.3390/s25216524
5. Zhang Y, Meng X, Shotorbani AM and Wang L. Minimization of AC-DC grid transmission loss and DC Voltage15 deviation using adaptive droop control and improved AC-DC power flow algorithm. in IEEE Transactions on16 Power Systems 2021; 36(1): 744–756. https://doi.org/10.1109/TPWRS.2020.3020039
6. Charadi S, Chaibi Y, Redouane A, Allouhi A, El Hasnaoui A and Mahmoudi H. Efficiency and energy-loss analysis18 for hybrid AC/DC distribution systems and microgrids: A review. Int Trans Electr Energ Syst 2021; 31(12): e13203. https://doi.org/10.1002/2050-7038.13203
7. Zhao T. Networked hybrid AC/DC microgrids with nonlinear conversion losses. IEEE Dataport August 7-2022.21. https://doi.org/10.21227/ayrv-ff02
8. Liserre M, Sauter T and Hung JY. Future energy systems: Integrating renewable energy sources into the23 smart power grid through industrial electronics. in IEEE Industrial Electronics Magazine 2010; 4(1): 18–37. https://doi.org/10.1109/MIE.2010.935861
9. Blaabjerg F, Yang Y, Kim KA and Rodriguez J. Power Electronics Technology for Large-Scale Renewable Energy Generation. in Proceedings of the IEEE 2023; 111(4): 335–355. https://doi.org/10.1109/JPROC.2023.3253165
10. Baros D, Voglitsis D, Papanikolaou NP, Kyritsis A and Rigogiannis N. Wireless power transfer for distributed energy sources exploitation in DC microgrids. in IEEE Transactions on Sustainable Energy 2019; 10(4): 2039–2049. https://doi.org/10.1109/TSTE.2018.2877902
11. Khaled O, Lutfi A, Usama I and Hasan M. Wireless power transfer: Applications, challenges, barriers, and the role of AI in achieving sustainable development goals - A bibliometric analysis. Energy Strategy Reviews 2024; 53(32): 101376. https://doi.org/10.1016/j.esr.2024.101376
12. Rahman MM, Shanto MSI, Sarker N, Rani T and Paul LC. A comprehensive review of wireless power transfer methods, applications, and challenges. Engineering Reports, 2024; 6(10): e12951. https://doi.org/10.1002/eng2.12951

13. Keller B, Buscher U. Single row layout models 2015; 245(3): 629–644. https://doi.org/10.1016/j.ejor.2015.03.016
14. Hamzeei M, Farahani RZ, Rashidi-Bejgan, H. An exact and a simulatedannealing algorithm for simultaneously determining flow path and the locationof p/d stations in bidirectional path 2013; 32(4): 648–654. https://doi.org/10.1016/j.jmsy.2013.07.002
15. Roodbergen KJ, Sharp GP, Vis, IFA. Designing the layout struc-ture of manual order picking areas in warehouses 2007; 40(11): 1032–1045. https://doi.org/10.1080/07408170802167639
16. Cheah WC, Watson SA, Lennox B. Limitations of wireless power transfer technologies for mobile robots. *Wireless Power Transfer* 2019; 6(2): 175–189. https://doi.org/10.1017/wpt.2019.8
17. Mou, X, Sun, H. Wireless Power Transfer: Survey and Roadmap. 2015 IEEE 81st Vehicular Technology Conference (VTC Spring):proceedings. Glasgow, Scotland, 11–14 May 2015. (pp. 1–5). Institute of Electrical and Electronics Engineers. https://doi.org/10.1109/vtcspring.2015.7146165
18. Rabih M, Takruri M, Al-Hattab M, Alnuaimi AA, Bin Thaleth MR. Wireless charging for electric vehicles: A survey and comprehensive guide. World Electr. Veh. J. 2024; 15: 118. https://doi.org/10.3390/wevj15030118
19. Abuajwa O, Thiagarajah SP, Ambak Z. *et al.* Comprehensive review of wireless power transfer systems for electric vehicle charging applications. *Discov Appl Sci* 2025; 7: 1176. https://doi.org/10.1007/s42452-025-07738-z
20. Latha B, Irfan MM, Reddy BK. *et al.* A novel enhancing electric vehicle charging: an updated analysis of wireless power transfer compensation topologies. *Discov Appl Sci* 2025; 7: 240. https://doi.org/10.1007/s42452-025-06630-0
21. Bin Hassan MN, Watson S, Zhang C. 2025. Resonant Inductive Coupling Power Transfer for Mid-Sized Inspection Robot. In: Huda, M.N., Wang, M., Kalganova, T. (eds) Towards Autonomous Robotic Systems. TAROS 2024. Lecture Notes in Computer Science, vol 15051. Springer, Cham. https://doi.org/10.1007/978-3-031-72059-8_20
22. Pairindra W, Phongsawat S, Phophongviwat T, Khomfoi S. The development of a 1 kW mid-range wireless power transfer platform for autonomous guided vehicle applications using an LCC-S resonant compensator. *World Electr. Veh. J.* 2025; *16*: 322. https://doi.org/10.3390/wevj16060322
23. Sokolovs A, Stepins D and Zakis J. Dynamic Wireless Power Transfer System for Multiple Automated Guided Vehicles. *2024 IEEE 11th Workshop on Advances in Information, Electronic and Electrical Engineering (AIEEE)*, Valmiera, Latvia, 2024, pp. 1–4, https://doi.org/10.1109/AIEEE62837.2024.10586691
24. Stepins D, Zakis J, Sokolovs A, Husev O, Strzelecki R and Doncker RWD. Dynamic wireless power transfer system for indoor AGV with a distance-measurement-based position detection technique. in *IEEE Access*, 2025; 13: 71551–71562. https://doi.org/10.1109/ACCESS.2025.3562134
25. Zeng J, Du X and Yang Z. A multiport bidirectional DC–DC converter for hybrid renewable energy system integration. in IEEE Transactions on Power Electronics 2021; 36(11): 12281–12291. https://doi.org/10.1109/TPEL.2021.3082427
26. Vinh NT, Nguyen VT, Van Dung N. et al, New flexible bidirectional converter for electric vehicle substations connecting microgrids, Sci Rep, 2025; 15: 35391. https://doi.org/10.1038/s41598-025-19277-z
27. Vinh NT and Dung NV. Flexible converter for electric vehicle charging station using renewable energy efficiently, International Journal of Technology, 2025; 16(5): 1800–1815. https://doi.org/10.14716/ijtech.v16i5.770
28. Sarvi M and Zohdi HZ. A comprehensive overview of DC-DC converters control methods and topologies in DC microgrids. Energy Sci Eng 2024; 12: 2017–2036. https://doi.org/10.1002/ese3.173041
29. Lee ES. Editorial on wireless power transfer (WPT): Present advancements, applications, and future outlooks. Applied Sciences 2024; 14(22): 10627. https://doi.org/10.3390/app142210627
30. Yao Y and Zhong W. General model and analysis of misalignment characteristics of fixed-frequency WPT systems. in IEEE Transactions on Power Electronics 2023; 38(11): 13315–13328. https://doi.org/10.1109/TPEL.2023.3301655